Nanoflake $NiMoO_4$ based smart supercapacitor for intelligent power balance monitoring

Harish. S. Chavan,[1] Bo Hou,[2] Abu Talha Aqueel Ahmed,[1] Yongcheol Jo,[1] Sangeun Cho,[1] Jongmin Kim,[1] Sambhaji M. Pawar,[1] SeungNam Cha,[2] Akbar I. Inamdar,*[1] Hyunsik Im,*[1] Hyungsang Kim*[1]

[1]*Division of Physics and Semiconductor Science, Dongguk University, Seoul 04620, South Korea*
[2]*Department of Engineering Science, University of Oxford, Parks Road, OX1 3PJ, UK*

A supercapacitor is well recognized as one of emerging energy sources for powering electronic devices in our daily life. Although various kind of supercapacitors have been designed and demonstrated, their market aspect could become advanced if the utilisation of other physicochemical properties (e.g. optical) is incorporated in the electrode. Herein, we present an electrochromic supercapacitor (smart supercapacitor) based on a nanoflake $NiMoO_4$ thin film which is fabricated using a facile and well-controlled successive ionic layer adsorption and reaction (SILAR) technique. The polycrystalline nanoflake $NiMoO_4$ electrode exhibits a large electrochemically active surface area of ~ 96.3 cm^2. Its nanoporous architecture provides an easy pathway for the intercalation and de-intercalation of ions. The nanoflake $NiMoO_4$ electrode is dark-brown in the charged state and becomes transparent in the discharged state with a high optical modulation of 57 %. The electrode shows a high specific capacity of 1853 Fg^{-1} at a current rate of $1Ag^{-1}$ with a good coloration efficiency of 31.44 cm^2/C. Dynamic visual information is obtained when the electrode is charged at different potentials, reflecting the level of energy storage in the device. The device retains 65% capacity after 2500 charge-discharge

cycles compared with its initial capacity. The excellent performance of the nanoflake $NiMoO_4$ based smart supercapacitor is associated with the synergetic effect of nanoporous morphology with a large electrochemically active surface area and desired chemical composition for redox reaction.

Keywords: $NiMoO_4$, nanoflake morphology, smart supercapacitor, SILAR technique.

Corresponding Authors

*E-mail: akbarphysics2002@gmail.com, hyunsik7@dongguk.edu, hskim@dongguk.edu

Introduction

Supercapacitors are promising energy storage devices because of their outstanding characteristics such as high power density, fast charging ability, and excellent electrochemical cycling stability [1–4]. The charge storage mechanism in electrochemical supercapacitors (pseudocapacitors) is associated with the reversible Faradaic reaction. Electrosorption or intercalation processes occur on the surface of an electrode accompanying an electron charge-transfer between electrolyte and electrode, and this reversible reaction often changes the color of the electrode (known as electrochromism) [5]. Devices having such dual functionality are called smart supercapacitors [5,6–19]. Smart supercapacitors store energy as a normal supercapacitor and sense the level of energy stored by changing visual color. Recently, diverse transition metal oxides (TMOs) and complex compounds have been investigated for use as smart supercapacitor electrodes.

A literature survey on the present status of the smart supercapacitor technology, based on TMOs and complex compounds, is presented in Figure 1, together with our results [5–19]. The

wavelength on the horizontal axis is associated with the color of the electrode materials in the colored state. Well-known materials such as WO_3 and its complex compounds, polyaniline (PANI), carbon nanotubes (CNT), and nickel oxide (NiO) have been investigated as smart supercapacitors. Attempts have been made to fabricate nanostructured materials to enhance the electrochemical reaction and efficiency using different techniques such as Rf-magnetron sputtering, electrodeposition, hydrothermal, thermal evaporation, spin coating, and chemical vapor deposition [6–19]. The techniques used for the synthesis of nanostructured materials need a long time and a sophisticated experimental setup. Thus, the challenge is to obtain a reliable electrode material that is abundant, non-toxic, and cost-effective, which can be fabricated using simple experimental techniques. Drawbacks, such as high production cost, low reversibility, short lifetime, low chromatic contrast, compromised capacity, and low coloration efficiency, need to be overcome. Based on the literature discussed, it has been noted that $NiMoO_4$, which is an abundant material and can be easily synthesized using chemical techniques, has not yet been employed for smart supercapacitor applications. It is anticipated that the electrochemical properties of $NiMoO_4$ will be satisfactory because Mo can enhance the conductivity of an electrode. There is also the high electrochemical activity of nickel ions.

In this work we report on the synthesis of a binder-free, nanoflake $NiMoO_4$ thin film electrode on an ITO coated conducting glass substrate by using the SILAR technique. The nanoflake $NiMoO_4$ electrode exhibits bifunctionalities for electrochemical energy storage and electrochromism. A maximum specific capacitance of 1853 Fg^{-1} at 1 Ag^{-1}, with good capacity retention over 2500 cycles, is obtained. During the charging and discharging processes, the electrode shows a color change between dark brown and transparent with good coloration efficiency of 31.44 cm^2/C.

Experimental

Nanoporous $NiMoO_4$ thin film electrodes were synthesized on ITO coated conducting glass substrates with a sheet resistance of 27 Ω cm^{-2} using the SILAR technique. A $NiMoO_4$ film was fabricated by successively dipping an ITO substrate in Ni and Mo solution baths (see Fig. S1 in Supplementary Information). One cycle consists of 20 s of dipping in the Ni-containing bath, 10 s in D. I. water, 20 s in the Mo-containing bath, and again, 10 s in D.I. water. Each bath contains 0.1 M $NiCl_2 \cdot 6H_2O$ and 0.1 M $Na_2MoO_4 \cdot 2H_2O$, respectively. The purpose of the water dipping step is to remove unwanted by-products. The pH of the Ni-containing bath is adjusted to 12.2 by dropwise addition of an ammonia solution. During the film deposition, the Mo- and Ni-containing baths were maintained at 70 °C and room temperature, respectively. Each cycle consists of ion adsorption and nucleation processes of both the Ni and Mo species at the substrate surface, resulting in the formation of composite $NiMoO_4$. The $NiMoO_4$ thin film was grown using 30 successive cycles. Subsequently, the film was annealed at 300 °C for 2 hours, to remove water content and to increase adhesion to the substrate. The thickness and active area of the electrode film are ~ 100 nm and 1×2 cm^2, respectively. The mass of the active electrode was estimated using a standard weight difference method and it is 0.17 mg.

The electrochemical supercapacitor and electrochromic performance of the $NiMoO_4$ thin film electrode were investigated using cyclic voltammetry (CV), galvanostatic charge/discharge, and AC impendence analysis. A potentiostat (Princeton Applied Research, Versa STAT 3) was used with a conventional three-electrode electrochemical cell containing a 2 M KOH electrolyte, $NiMoO_4$ as the working electrode, a saturated calomel electrode (SCE) as the reference electrode, and graphite as the counter-electrode. Electrochemical impedance spectroscopy (EIS) measurements were performed from 1 Hz to 10 kHz (AC), using an impedance analyzer. X-ray

diffraction (XRD) patterns of the films were recorded using an X-ray diffractometer with Ni-filtered Cu-Kα radiation (Ka α-1.54056 Å) (X pert PRO, Panalytical).

Surface morphology was observed using field emission scanning electron microscopy (FE-SEM, model: JSM-6701F, JEOL, Japan). The chemical states of the $NiMoO_4$ film were investigated using X-ray photoelectron spectroscopy (XPS, Ulvac -phi, Verse probe II). The microscopic structural properties of the sample were investigated using transmission electron microscopy (JEOL 3000F) and high angle annular dark field (HAADF) scanning transmission electron microscopy (STEM) with an Oxford EDX detector (JEM-2100), high-resolution transmission electron microscopy (HR-TEM), and selected area electron diffraction (SAED) were performed on JEOL 3000F at 300 kV. Optical transmittance is analyzed using a spectrophotometer.

Results and Discussion

The crystal structure of the as-prepared nanoflake $NiMoO_4$, heated to 300 °C, is determined through the X-ray diffraction spectrum. Figure 2(a) shows the X-ray diffraction spectrum of $NiMoO_4$ nanoflake thin film. The film consists of multiple diffraction peaks revealing its polycrystalline nature. The peaks marked with a star symbol are associated with the ITO substrate. The diffraction peaks observed at 23.08°, 45.26°, 55.68°, 60.26°, 62.02°, and 77.76° are assigned to the $(02\bar{1})$, (113), $(53\bar{2})$, (620), $(44\bar{3})$, and $(82\bar{2})$ Bragg indexes of a $NiMoO_4$ structure (JCPDS card # 45-0142), suggesting the formation of a $NiMoO_4$ structure. The polycrystalline nature which provides grain boundaries and granular voids for electrolyte penetration could improve the electrochemical performance of the electrode [5]. To further identify the formation of $NiMoO_4$, Raman spectroscopy analysis is performed. As shown in the

Figure 2 (b), two major peaks at 482 and 813 cm^{-1}, which correspond to Mo-O vibrations and Mo=O stretching modes of $NiMoO_4$, respectively [20,21], supporting the formation of $NiMoO_4$. Broad shoulder peaks observed at around 360 and 704 cm^{-1} are ascribed to the asymmetric stretching modes of Ni-O-Mo bonds [22].

The scanning electron microscopic image of the $NiMoO_4$ electrode is shown in Fig. 2(c) and Supplementary Fig. S2, revealing an interconnected nanoporous network of nanoflakes. The nanoporosity of the electrode can allow the electrolyte to penetrate through the electrode. This nanoporous architecture is expected to provide a high surface area and easy pathway for ion intercalation and de-intercalation. The uniform distribution of the main constituent elements (Ni, Mo, and O) is also confirmed by energy dispersive analysis measurements (supporting information, Fig. S3).

Figure 3 shows the HRTEM, SAED, and HAADF-STEM elemental mapping results of the $NiMoO_4$ thin film electrode. The HRTEM (Fig.3 (a)) image clearly resolves lattice fringes of nanoflake $NiMoO_4$. A lattice distance (d_{222}) of 0.22 nm (Fig.3 (b)) is indexed to the {222} plane, which is associated with the $NiMoO_4$ monoclinic crystal configuration. The SAED image in Fig. 3(c) shows multiple diffused diffraction rings, which correspond to the $(02\bar{1})$, $(02\bar{2})$, and (201) reflections. The appearance of the diffused rings is typical of polycrystalline materials [23]. Figure 3(d) shows the HAADF-STEM elemental mapping images of nanoflake $NiMoO_4$, which clearly demonstrates the homogeneous distributions of Ni, Mo, and O elements. The HAADF-STEM elemental line scan (1 μm) and EDS spectrum (Fig. S4, Supplementary information) further confirms the stoicheiometrically presence of Ni, Mo, and O. The atomic ratio of Ni:Mo is determined using EDAX, and it is found to be 1:0.45.

The presence of the constituent elements and the chemical states of the $NiMoO_4$ film are confirmed using X-ray photoelectron spectroscopy (XPS) analysis. Figure 4 displays the wide-scan survey spectrum, and Ni 2p, Mo 3d, and O 1s core-level spectra of the nanoflake $NiMoO_4$ film. To determine the peak positions in the core-level spectra, the Gaussian-Lorentz distribution function is used. The survey spectrum in Fig. 4(a) reveals the presence of elemental Ni, Mo, and O in the prepared material. For the core-level Ni 2p spectrum in Fig 4 (b), the binding energy peaks at 854.75 and 872.5 eV and their satellite peaks are associated with Ni^{2+} binding states of Ni $2p_{3/2}$ and Ni $2p_{1/2}$ [22, 24, 25]. The difference between these two peaks is 17.75 eV, which is related to the formation of Ni^{2+} oxidation states [24, 26]. In the Mo 3d core-level spectrum (shown in Fig.4 (c)), the peaks at 231.12 and 234.25 eV are associated with Mo $3d_{5/2}$ and Mo $3d_{3/2}$, respectively. The difference between these two peaks is 3.13 eV, which corresponds to Mo^{6+} oxidation states in the film [22, 24]. The peak at 530.5 eV in the O 1s spectrum (Fig 4(d)) is linked with metal-oxide bonds [24, 27].

The electrochromic properties of the $NiMoO_4$ nanoflakes electrode are now discussed. Figure 5 (a) shows a cyclic voltammetry (CV) curve of the $NiMoO_4$ nanoflake electrode at a scan rate of 5 mV/s. The arrow indicates the scan direction during the CV measurement. The pair of redox peaks observed in the CV is an indication of the pseudocapacitive behavior of the electrode. During the anodic scan, an oxidation peak is observed at 0.49V (vs SCE), and the film's color changes to dark brown. For the cathodic scan, the reduction peak appears at 0.18 V (vs SCE), and the film becomes transparent. Both the electrochromic performance and the pseudocapacitive behavior are based on the same mechanism, oxidation and reduction (redox reactions) between Ni^{2+} and Ni^{3+} states. The scan rate dependent CV curves are shown in Fig. S5 (Supplementary information). As the scan rate increases, the oxidation and reduction peaks shift.

This shift is due to the internal resistance of the electrode. The CV shape, even at a high scanning rate of 50 mV/s, remains similar, suggesting that the electrochemical reaction during charge/discharge processes is stable. The coloration (charging) and bleaching (discharging) are associated with the insertion and de-insertion of OH^- ions according to the following equation;

$$NiO + OH^- \leftrightarrow NiOOH + e^- \quad (1)$$

The reversible transition between NiO and NiOOH accompanies the charge transfer between Ni^{2+} and Ni^{3+} [3, 28, 29]. The charging and discharging processes are due to the charge transfer of Ni species. These processes are not due to Mo species because the oxidation state of Mo is +6. Mo does not undergo any charge transformation upon OH^- ion intercalation during the charging process. Even in the reverse potential scan, Mo does not undergo the reduction process because of the limited potential window. The intercalation of the OH^- ion causes the electrode to be in the charged state, with de-intercalation in the discharged state. The charged and discharged states of the electrode can be easily judged by observing the change in color.

The coloring performance of the $NiMoO_4$ nanoflake electrode is evaluated using optical transmittance measurements. The $NiMoO_4$ electrode is colored and bleached at ± 0.6 V (vs. SCE) for 30 s. The transmittance spectra of the $NiMoO_4$ electrode in the colored and bleached states are presented in Figure 5(b). The transmittance difference between the colored and bleached states gives information on the coloration efficiency of the electrode. The change in the optical density (ΔOD) at 630 nm is calculated using the following formula;

$$(\Delta \mathrm{OD})_{630\mathrm{nm}} = \log\left(\frac{Tb}{Tc}\right) \quad (2)$$

where T_b and T_c are the transmittances of the bleached and colored states. The electrode is ~ 93 % transparent in its original state, but the transparency decreases to 36.23 % in the fully charged state. The sample shows highly reversible color/bleach transmittance characteristics between the

bleached (transparent) and colored states with an optical modulation of ~ 57 % at 630nm. The (ΔOD) at 630 nm for the $NiMoO_4$ nanoflake electrode is found to be 0.9440. This obtained ΔOD can be used for the estimation of coloration efficiency (CE), which is defined as the change in the optical density per unit charge inserted into the electrochromic film. The following formula is used to calculate the coloration efficiency [7]:

$$CE_{630nm} = \left(\frac{(\Delta OD)630nm}{Q/A}\right) \quad (3)$$

where Q/A is the per unit charge density. The charges inserted into the electrochromic film are estimated from chronocoulometry (CC) measurements, shown in Figure 5 (c). The total charge per unit area for the film, which is colored at 0.6 V (vs SCE), is measured to be 30.01 mC. Thus, the coloration efficiency of the $NiMoO_4$ nanoflake electrode is calculated to be 31.44 cm^2/C.

Figure 5(c) shows the CC curves measured at different potentials. During the initial 60 (fixed time) seconds, the film becomes colored with a positive potential due to the intercalation of OH^- ions. Subsequently, the film becomes bleached with a negative potential for the next 60 seconds. Photographs of as-grown and colored films at different potentials are shown in Figure 5 (d). As the intercalated charges increases, the film becomes dark-brown. The film becomes transparent at the discharged state. Thus, the remaining energy level can be easily visualized through a simultaneous change in color with varying voltage.

The Electrochemically active surface area (ECSA) is estimated by measuring scan-rate dependent CV curves in the non-Faradaic voltage region, which is described by charge accumulation rather than redox reaction (Supplementary Figure S5) [30, 31]. A linear increase of the capacitive current with respect to the scan rate is observed. Figure 6 (a) shows the non-

Faradaic region of the CV curves at different scan rates. The ECSA for the nanoflake $NiMoO_4$ sample is estimated using the following expression [30, 31]:

$$ECSA = \frac{C_{DL}}{C_s} \quad (4)$$

where Cs is the specific capacitance of the electrolyte, and C_{DL} is the double-layer region specific capacitance. Cs = 0.040 $mFcm^{-2}$ for the KOH electrolyte [31]. The capacitive current (I_{DL}) at different scan rates is estimated from the non-faradic region, as follows:

$$I_{DL} = C_{DL} \times \nu \quad (5)$$

Figure 6(b) shows the capacitive current (I_{DL}) of the nanoflake $NiMoO_4$ electrode. Figure 6(c) shows the current at 0.21 V, as a function of scan rate (ν). The C_{DL} is the slope of the curve. The ECSA value for the $NiMoO_4$ electrode is calculated to be ~ 96.3 cm^2.

The electrochemical supercapacitor properties of the $NiMoO_4$ nanoflake electrode are now investigated. Figure 7(a) shows its galvanostatic charge-discharge (CD) properties at different current densities. The non-linear and symmetric behavior of the charge-discharge curves suggests the pseudocapacitive nature of the electrode [5]. During the charging and discharging processes, the voltage plateaus at around 0.25 and 0.18 V (vs SCE), associated with the oxidation and reduction processes, respectively. The film is brown in the fully charged state and transparent in the fully discharged state. The specific capacity is calculated using the following equation;

$$Cs = I\Delta t / m\Delta V \quad (6)$$

where Cs is the specific capacitance, and *I* and *m* represent the discharge current and the mass of active materials, respectively. ΔV and Δt are the potential window and total discharge time, respectively. The specific capacitance, obtained at different current densities, is presented in

Figure 7 (b). The specific capacitance decreases gradually with increasing discharge current density. This decrease is associated with ions diffusing and migrating into the active material. The specific capacitance (1853 Fg^{-1}), obtained for the nanoflake $NiMoO_4$ electrode, is much higher than the specific capacitance obtained from other smart supercapacitor electrodes (literature survey, summarized in Figure 1). The higher electrochemical capacitance of the $NiMoO_4$ nanoflake electrode is associated with the synergetic effect between nanostructure morphology which provides easy path way for the ion diffusion, chemical composition for the desired redox reactions, and shorter diffusion length for the faster kinetics.

The CV curves measured at different scan rates are used to estimate the scan rate dependent specific capacitance of the $NiMoO_4$ nanoflake electrode using the following formula,

$$Cs = \int (IdV)/(2m \times \nu \times \Delta V) \quad (7)$$

where Cs is specific capacitance and *IdV* is the area under the curve. Figure S5 shows the scan rate dependent specific capacity of the $NiMoO_4$ nanoflake electrode. The specific capacity of the $NiMoO_4$ nanoflake electrode is 937 F/g, and it decreases with increasing scan rate.

Electrochemical cycling stability of the nanoflake $NiMoO_4$ electrode is evaluated at a high current density of 10 Ag^{-1} for 2500 cycles. Figure 7(c) shows the specific capacitance as a function of cycle number. The specific capacitance decreases gradually as the cycle number increases. The capacitance after the 2500th cycle is 301 Fg^{-1}, which is 65 % retention of the initial capacity. A gradual decrease in specific capacity can be from structural damage to an electrode, which increases the electrical resistance of the electrode [32, 33].

The coulombic efficacy η of the $NiMoO_4$ nanoflake electrode is estimated using the following expression:

$$\eta = Td / Tc \times 100 \quad (8)$$

where Td is the discharge time and Tc is the charge time. Figure 7(c) represents the measured coulombic efficiency as a function of cycle number. The overall coulombic efficiency of the sample is larger than 95%, revealing their excellent cycling performance and reversibility.

Figure 7(d) shows a Nyquist plot of the nano-flake $NiMoO_4$ electrode, before and after 2500 charge-discharge cycles along with equivalent circuit diagram. The Nyquist plots are recorded in the frequency range of 1Hz to 10 kHz. Nyquist plots consist of a semicircle in the high-frequency region and slight straight line in the low-frequency region, which are attributed to the charge transfer resistance (R_{ct}) and Warburg impedance W of the electrode material, respectively. The intersection of the semicircle in the x-axis indicates the internal resistance of the electrodes (R_s), which is a combination of the intrinsic resistance of the substrate and electrolyte resistance of the electrochemical system, CPE is the constant phase element. The fitted impedance parameters are provided in supplementary table S1. The R_s value of the nano-flake $NiMoO_4$ electrode before and after cycling are 44.66 and 48.38Ω, respectively indicating constancy of the electrochemcial system used to estimate impedance data. The charge-transfer resistance (R_{ct}) of the electrode is found to be 42.69 and 75.08 Ω before and after cycling respectively. The increased electrochemical resistance with cycle number is associated with the structural reconstruction of the nano-flake $NiMoO_4$ electrode during charge-discharge processes.

The power (P) and energy (E) densities (Ragone plot) are calculated from the charge/discharge measurements, using the following equations:

$$E = 0.5 \times Cs \times \Delta V^2 \tag{9}$$

$$P = E/\Delta t \tag{10}$$

Figure 8 shows a Ragone plot for power (P) and energy (E) densities of the nanoflake $NiMoO_4$ electrode. The energy density decreases with increasing power density, exhibiting a high energy density of 117 Wh/kg at a given power density of 7527 W/kg compared with other oxide materials [34,35]. The steep slope in the P-E plot indicates the electrode's superior supercapacitive performance, even at high current rates.

Conclusions

For the first time, we successfully demonstrate a balance-visualized smart supercapacitor via employing electrochromic nanoflake $NiMoO_4$. A facile and robust synthetic strategy is developed for the growth of a polycrystalline nanoflake $NiMoO_4$ nanostructure. A high specific capacitance of 1853 Fg^{-1} at a current density of 1 Ag^{-1} is obtained, with good coloration efficiency of 31.44 cm^2/C. The nanoflake $NiMoO_4$ electrode can generate an energy density of 117 Wh/kg at a power density of 7527 W/kg. The electrode also shows stable long-cycle performance over 2500 charge-discharge cycles. The as-prepared electrode exhibits fast and reversible color modulation between the charged (dark-brown) and discharged (transparent) states which offers dynamic visual information on the status of power storage. Our findings suggest an efficient pathway for material design for high-performance intelligent multi-functional electrochemical energy storage devices. The $NiMoO_4$ nanoflake electrode would be excellent capacitor and good counter electrode in WO_3-based electrochromic devices where both electrodes contribute to the coloration.

Acknowledgements

The authors would like to thank the financial support from the National Research Foundation (NRF) of Korea (Grant nos. 2015M2A2A6A02045251, 2018R1A2B6007436, 2016R1A6A1A03012877, and 2015R1D1A1A01060743).

References

[1] P. Simon, Y. Gogotsi, B. Dunn, Where Do Batteries End and Supercapacitors Begin?, Science 343 (2014) 1210.

[2] X. H. Xia, D. L. Chao, Z. X. Fan, C. Guan, X. H. Cao, H. Zhang, H. J. Fan, A New Type of Porous Graphite Foams and Their Integrated Composites with Oxide/Polymer Core/Shell Nanowires for Supercapacitors: Structural Design, Fabrication, and Full Supercapacitor Demonstrations, Nano Lett. 14 (2014) 1651–1658.

[3] J. Q. Sun, W. Y. Li, B. J. Zhang, G. Li, L. Jiang, Z. G. Chen, R. J. Zou, J. Q. Hu, 3D core/shell hierarchies of MnOOH ultrathin nanosheets grown on NiO nanosheet arrays for high-performance supercapacitors, Nano Energy 4 (2014) 56–64.

[4] D. T. Dam, X. Wang, J. M. Lee, Mesoporous ITO/NiO with a core/shell structure for supercapacitors, Nano Energy 2 (2013) 1303–1313.

[5] P. Yang, P. Sun, Z. Chai, L. Huang, X. Cai, S. Tan, J. Song, and W. Mai, Large-Scale Fabrication of Pseudocapacitive Glass Windows that Combine Electrochromism and Energy Storage, Angew. Chem. Int. Ed. 53 (2014) 11935 –11939.

[6] G. Cai, X. Wang, M. Cui, P. Darmawan, J. Wang, A. L. S. Eh, P. S. Lee, Electrochromo-supercapacitor based on direct growth of NiO nanoparticles, Nano Energy 12 (2015) 258–267.

[7] A. I. Inamdar, J. Kim, Y. Jo, H. Woo, S. Cho, S. M. Pawar, S. Lee, J. L. Gunjakaa, Y. Cho, B. Hou, S. Cha, J. Kwak, Y. Park, H. Kim, H. Im, Highly efficient electro-optically tunable smart-supercapacitors using an oxygen-excess nanograin tungsten oxide thin film, Sol. Energy Mater. Sol. Cells 166 (2017) 78–85.

[8] D. Wei, M. R. J. Scherer, C. Bower, P. Andrew, T. Ryhanen, U. Steiner, A Nanostructured Electrochromic Supercapacitor, Nano Lett. 12 (2012) 1857−1862.

[9] Y. Tian, S. Cong, W. Su, H. Chen, Q. Li, F. Geng, Z. Zhao, Synergy of $W_{18}O_{49}$ and Polyaniline for Smart Supercapacitor Electrode Integrated with Energy Level Indicating Functionality, Nano Lett. 14 (2014) 2150−2156.

[10] T. Gwang, Y. D. Kim, Y. H. Kim, M. Park, S. Hyun, S. M. Han, Photoresponsive Smart Coloration Electrochromic Supercapacitor, Adv. Mater. 29 (2017) 1606728.

[11] K. Li, Y. Shao, S. Liu, Q. Zhang, H. Wang, Y. Li, R. B. Kaner, Aluminum-ion-intercalation supercapacitors with ultrahigh areal capacitance and highly enhanced cycling stability: Power supply for flexible electrochromic devices, small 13 (2017) 1700380.

[12] L. Shen, L. Du, S. Tan, Z. Zang, C. Zhao, W. Mai, Flexible electrochromic supercapacitor hybrid electrodes based on tungsten oxide films and silver nanowires, Chem. Commun. 52 (2016) 6296–6299.

[13] X. Chen , H. Lin , P. Chen , G. Guan, J. Deng , H. Peng, Smart, Stretchable Supercapacitors, Adv. Mater. 26 (2014) 4444–4449.

[14] X. Chen, H. Lin, J. Deng, Y. Zhang, X. Sun, P. Chen, X. Fang, Z. Zhang, G. Guan, H. Peng, Electrochromic Fiber-Shaped Supercapacitors, Adv. Mater. 26 (2014) 8126–8132.

[15] G. Cai, P. Darmawan, M. Cui, J. Wang, J. Chen, S. Magdassi, P. S. Lee, Supercapacitors: Highly Stable Transparent Conductive Silver Grid/PEDOT: PSS Electrodes for Integrated Bifunctional Flexible Electrochromic Supercapacitors, Adv. Energy Mater. 6 (2016) 1501882.

[16] C. Liu, X. Liu, H. Xuan, J. Ren, L. Ge, A Smart Colorful Supercapacitor with One Dimensional Photonic Crystals, Scientific Reports 5 (2015) 18419.

[17] W. Dong, Y. Lv, N. Zhang, L. Xiao, Y. Fan, X. Liu, Trifunctional NiO–Ag–NiO electrodes for ITO-free electrochromic supercapacitors, J. Mater. Chem. C 5 (2017) 8408–8414.

[18] F. Grote, Z. Yu, J-L. Wang, S-H. Yu, Yong Lei, Self-Stacked Reduced Graphene Oxide Nanosheets Coated with Cobalt–Nickel Hydroxide by One-Step Electrochemical Deposition toward Flexible Electrochromic Supercapacitors, small 11 (2015) 4666–4672.

[19] L. Zhu, C. Kang, N. Peh, T. Zhu, Y-F. Lim, G. W. Ho, Bifunctional 2D-on-2D MoO_3nanobelt/$Ni(OH)_2$ nanosheets for supercapacitor-driven electrochromic energy storage, J. Mater. Chem. A, 5 (2017) 8343–8351.

[20] Y. Y. Chen, Y. Zhang, X. Zhang, T. Tang, H. Luo, S. Niu, Z-H. Dai, L. J. Wan, J-S. Hu, Self-Templated Fabrication of $MoNi_4/MoO_3$-xNanorod Arrays with Dual Active Components for Highly Efficient Hydrogen Evolution, Adv. Mater. (2017) 1703311.

[21] E. Israel, Wachs, A.Charles, Roberts, Monitoring surface metal oxide catalytic active sites with Raman spectroscopy, Chemical Society Reviews 39 (2010) 5002–5017.

[22] P. R. Jothi, K. Shanthi, R. R. Salunkhe, M. Pramanik, V. Malgras, S. M. Alshehri, Y. Yamauchi, Synthesis and Characterization of α-$NiMoO_4$ Nanorods for Supercapacitor Application, Eur. J. Inorg. Chem. (2015) 3694–3699.

[23] B. Hou, Y. Cho, B. S. Kim, D. Ahn, S. Lee, J. B. Park, Y. W. Lee, J. Hong, H. Im, S. M. Morris, J. I. Sohn, S. N. Cha, J. M. Kim, Red green blue emissive lead sulfide quantum dots: heterogeneous synthesis and applications, J. Mater. Chem. C, 5 (2017) 3692–3698.

[24] K. Xiao, L. Xia, G. Liu, S. Wang, L-X Ding, H. Wang. Honeycomb-like $NiMoO_4$ ultrathin nanosheet arrays for high-performance electrochemical energy storage, J. Mater. Chem. A 3 (2015) 6128–6135.

[25] A. I. Inamdar, R. S. Kalubarme, J. Kim, Y. Jo, H. Woo, S. Cho, S. M. Pawar, Chan-Jin Park, Young-Woo Lee, J. I. Sohn, S. Cha, J. Kwak, H. Kim, H. Im, Nickel titanate lithium-ion battery anodes with high reversible capacity and high-rate long-cycle life performance, J. Mater. Chem. A 4 (2016) 4691–4699.

[26] S. Saha, M. Jana, P. Khanara, P. Samanta, H. Koo, N. C. Murmu, T. Kuila, Band gap modified boron doped NiO/Fe_3O_4 nanostructure as the positive electrode for high energy asymmetric supercapacitors, RSC Adv. 6 (2016) 1380–1387.

[27] Z. Yin, S. Zhang, Y. Chen, P. Gao, C. Zhu, P. Yang, L. Qi, Hierarchical nanosheet-based $NiMoO_4$ nanotubes: synthesis and high supercapacitor performance, J. Mater. Chem. A 3 (2015) 739–745.

[28] A. C. Sonavane, A. I. Inamdar, P. S. Shinde, H. P. Deshmukh, R. S. Patil, P. S. Patil, Efficient electrochromic nickel oxide thin films by electrodeposition, Journal of Alloys and Comp. 489 (2010) 667–673.

[29] M. M. Uplane, S. H. Mujawar, A. I. Inamdar, P. S. Shinde, A. C. Sonavane, P. S. Patil, Structural, optical and electrochromic properties of nickel oxide thin films grown from electrodeposited nickel sulphide, Applied Surface Sci. 253 (2007) 9365–9371

[30] V. Kannan, A. I. Inamdar, S. M. Pawar, H. S. Kim, H. C. Park, H. Kim, H. Im, Y. S. Chae, Facile Route to NiO Nanostructured Electrode Grown by Oblique Angle Deposition Technique for Supercapacitors, ACS Appl. Mater. Interfaces 8 (2016) 17220−17225.

[31] C. C. McCrory, S. Jung, J. C. Peters, T. F. Jaramillo, Benchmarking heterogeneous electrocatalysts for the oxygen evolution reaction, J. Am. Chem. Soc. 135 (2013) 16977−16987.

[32] M. C. Liu, L. B. Kong, C. Lu, X. J. Ma, X. M. Li, Y. C. Luo, L. Kang, Design and synthesis of $CoMoO_4$–$NiMoO_4.xH_2O$ bundles with improved electrochemical properties for supercapacitors, J. Mater. Chem. A 1 (2013) 1380−1387.

[33] J. Y. Lei, Z. Q. Jiang, X. F. Lu, G. D. Nie, C. Wang, Synthesis of Few-Layer MoS_2 Nanosheets-Wrapped Polyaniline Hierarchical Nanostructures for Enhanced Electrochemical Capacitance Performance, Electrochim. Acta 176 (2015) 149–155.

[34] L. Zhao, J. Yu, W. Li, S. Wang, C. Dai , J. Wu, X. Bai, C. Zhi, Honeycomb porous MnO_2 nanofibers assembled from radially grown nanosheets for aqueous supercapacitors with high working voltage and energy density, Nano Energy 4 (2014) 39–48.

[35] L. An, K. Xu, W. Li, Q. Liu, Bo Li, R. Zou, Z. Chen and J. Hu, Exceptional pseudocapacitive properties of hierarchical NiO ultrafine nanowires grown on mesoporous NiO nanosheets, J. Mater. Chem. A 2 (2014) 12799.

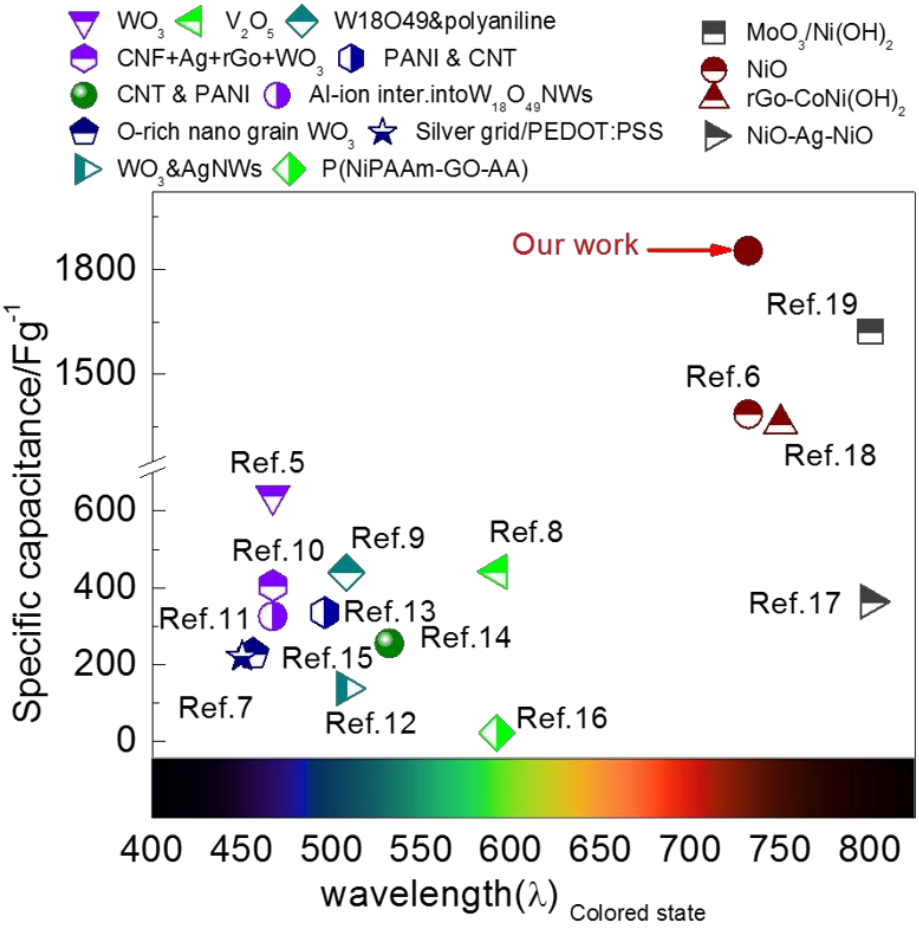

Fig. 1. Schematic representation of the materials used for the smart supercapacitor technology, exhibiting their specific capacities, compared with the present work.

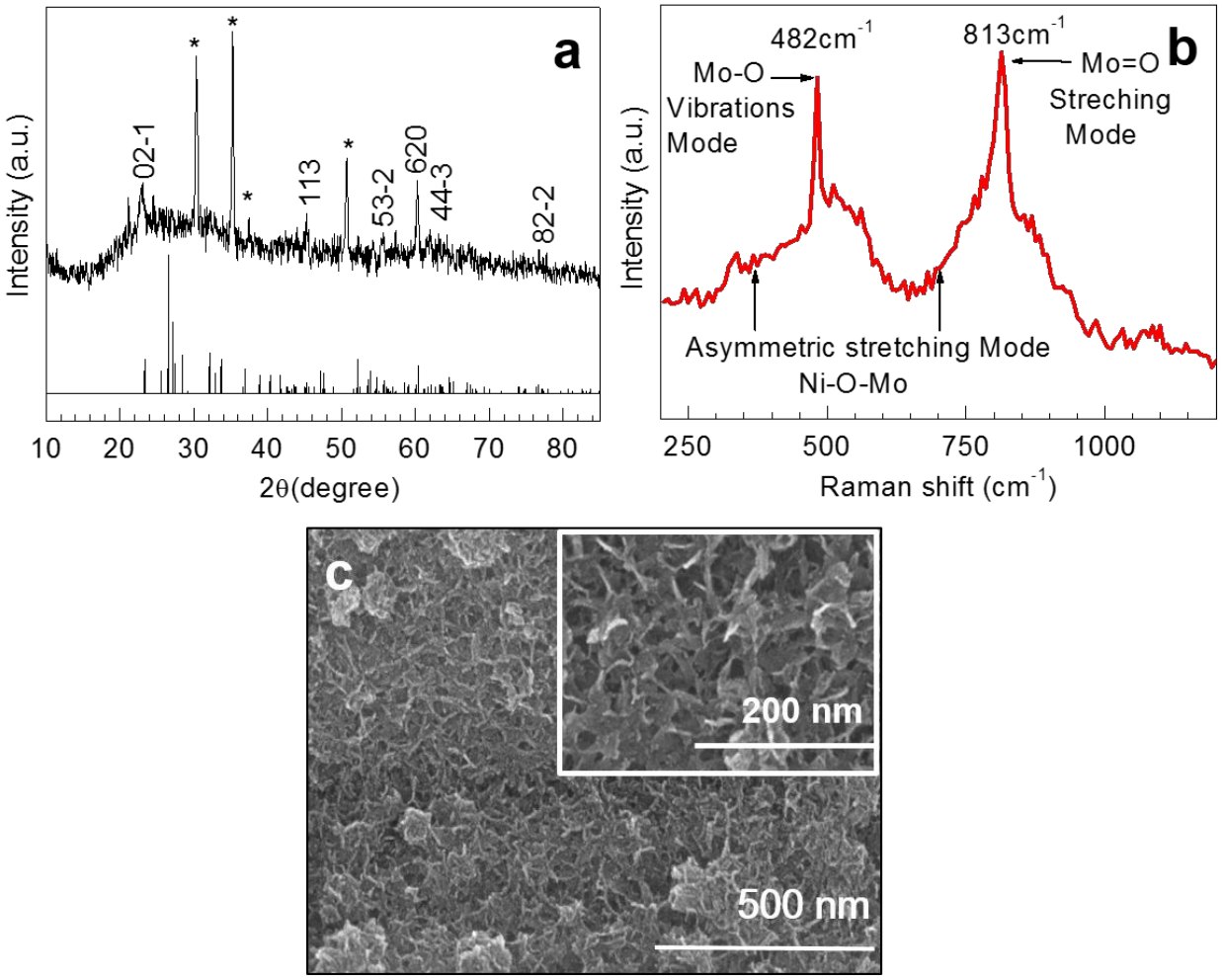

Fig. 2. (a) X-ray diffraction pattern of the $NiMoO_4$ film, along with the standard JCPDS (45-142) data. The star symbol (*) indicates the signal from the ITO substrate. (b) Raman spectrum of the $NiMoO_4$ film, showing two main peaks associated with Mo–O vibration and Mo=O stretching modes of the $NiMoO_4$ structure. (c) SEM image of the $NiMoO_4$ film, showing a unique nanoflake morphology.

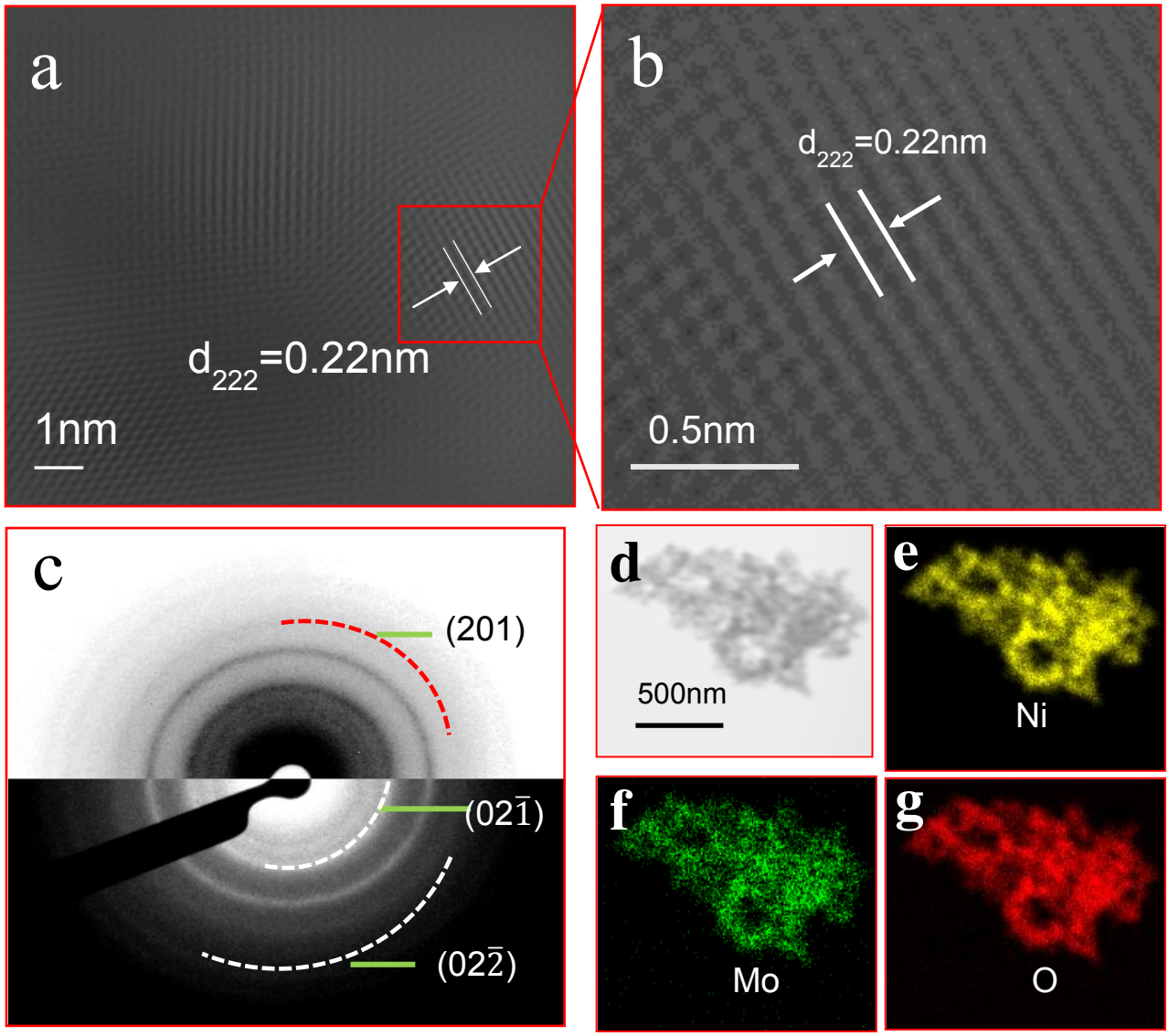

Fig. 3. (a) HRTEM image of the nanoflake $NiMoO_4$, (b) HRTEM image showing lattice fringes, (c) selective area electron diffraction (SAED) pattern, and (d-g) HAADF-STEM image of nanoflake $NiMoO_4$ and elemental mapping under the TEM mode, revealing the homogeneous distributions of Ni, Mo, and O in the nanoflake $NiMoO_4$.

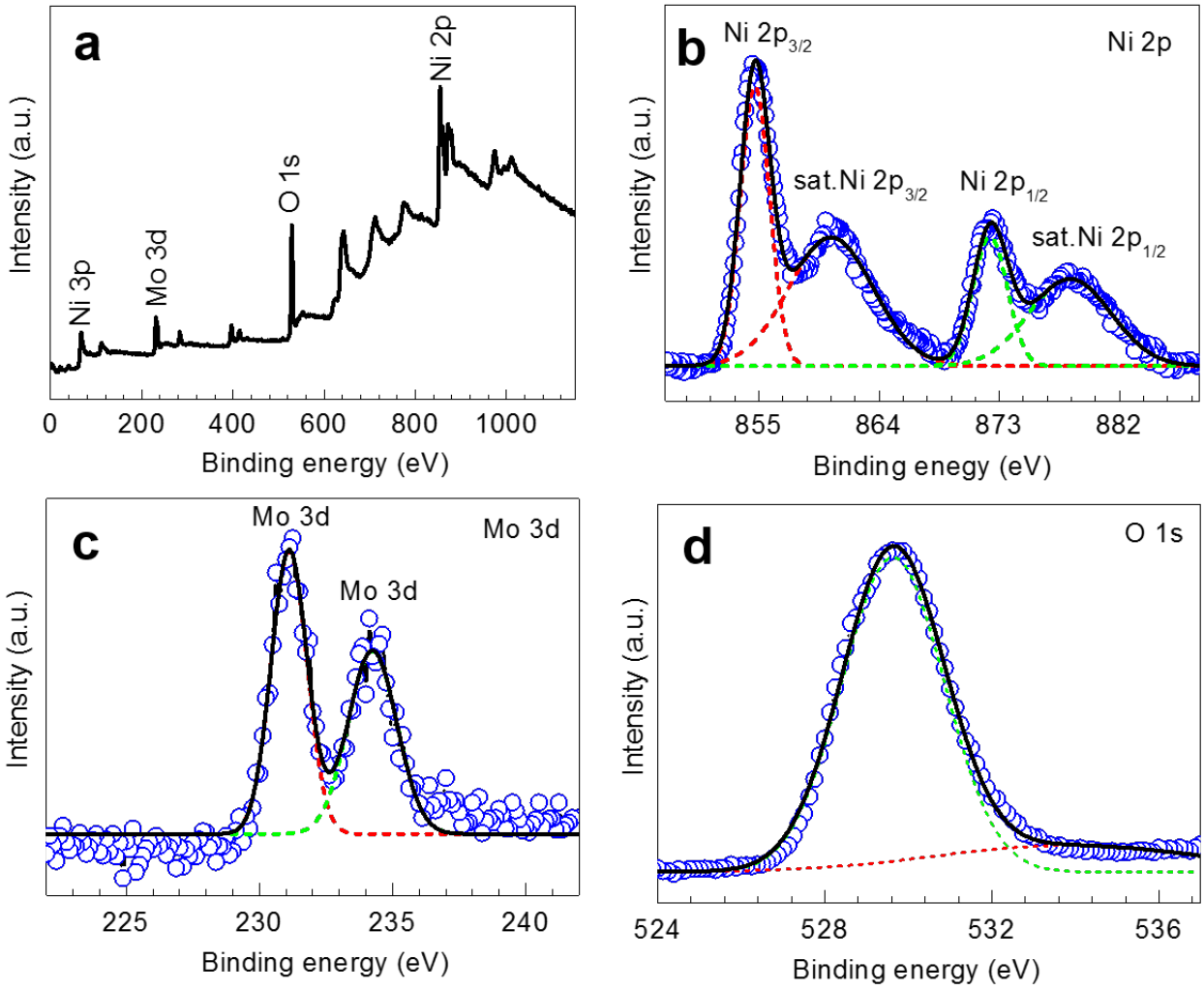

Fig. 4. XPS spectra of $NiMoO_4$: (a) Survey scan revealing the existence of Ni, Mo, and O as constituent elements. A high-resolution scan of the (b) Ni 2p peaks, (c) Mo 3d peaks, and (d) O 1s peaks. The solid circles and lines represent the experimental data and fitting curves, respectively.

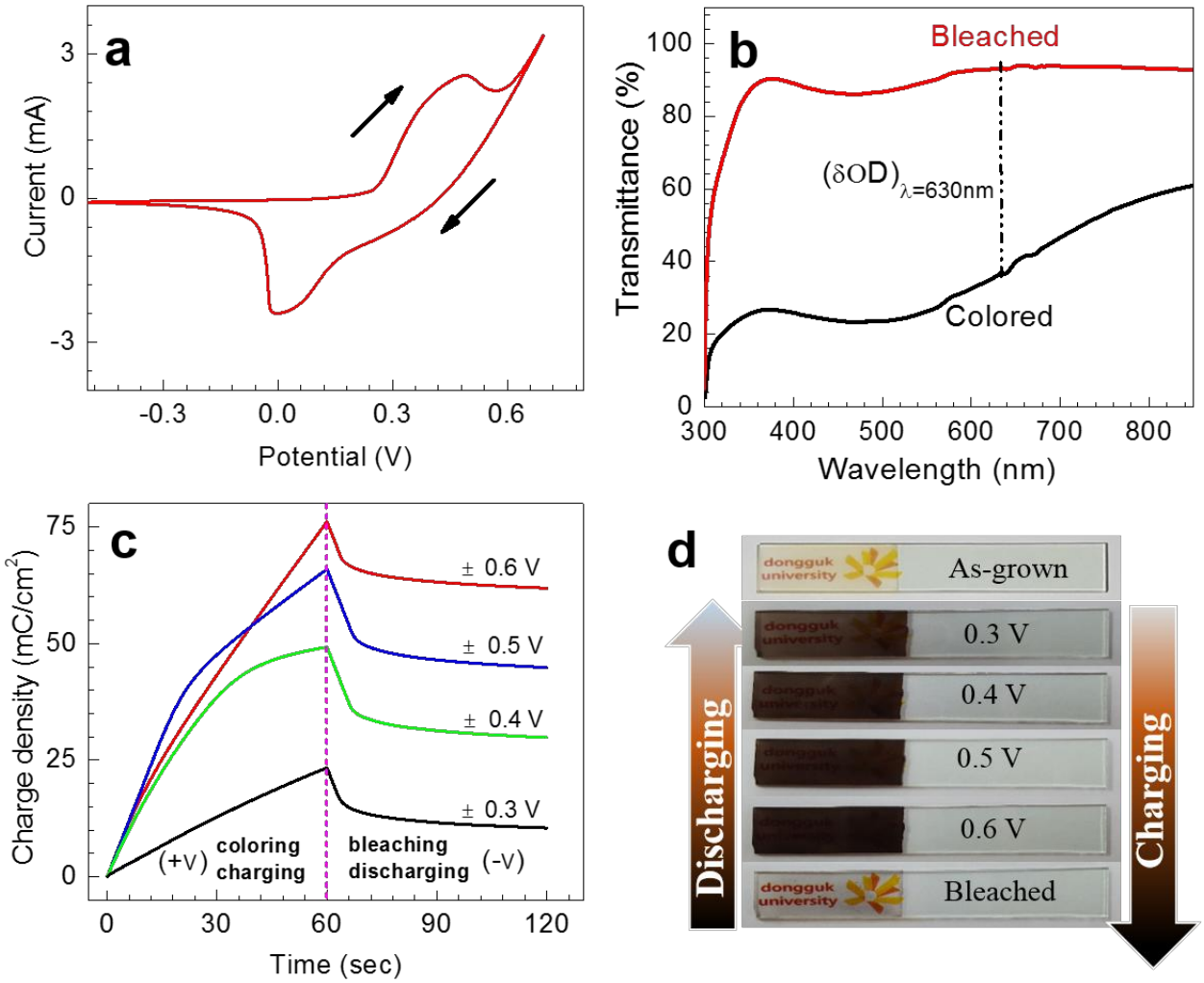

Fig. 5. (a) Cyclic Voltammogram of the $NiMoO_4$ electrode, recorded in a 2M KOH electrolyte at a scan rate of 5mV/s, (b) Optical transmittance spectra for the $NiMoO_4$ electrode in the colored and bleached states. (c) Chronocoulometry measurements for the film, colored at ± 0.3, 0.4, 0.5 and 0.6 V, (d) Actual photographic image of the $NiMoO_4$ electrode bleached at – 0.6 V vs. SCE, and at 0.3, 0.4, 0.5, and 0.6 V vs. SCE. These states are associated with different levels of stored charge.

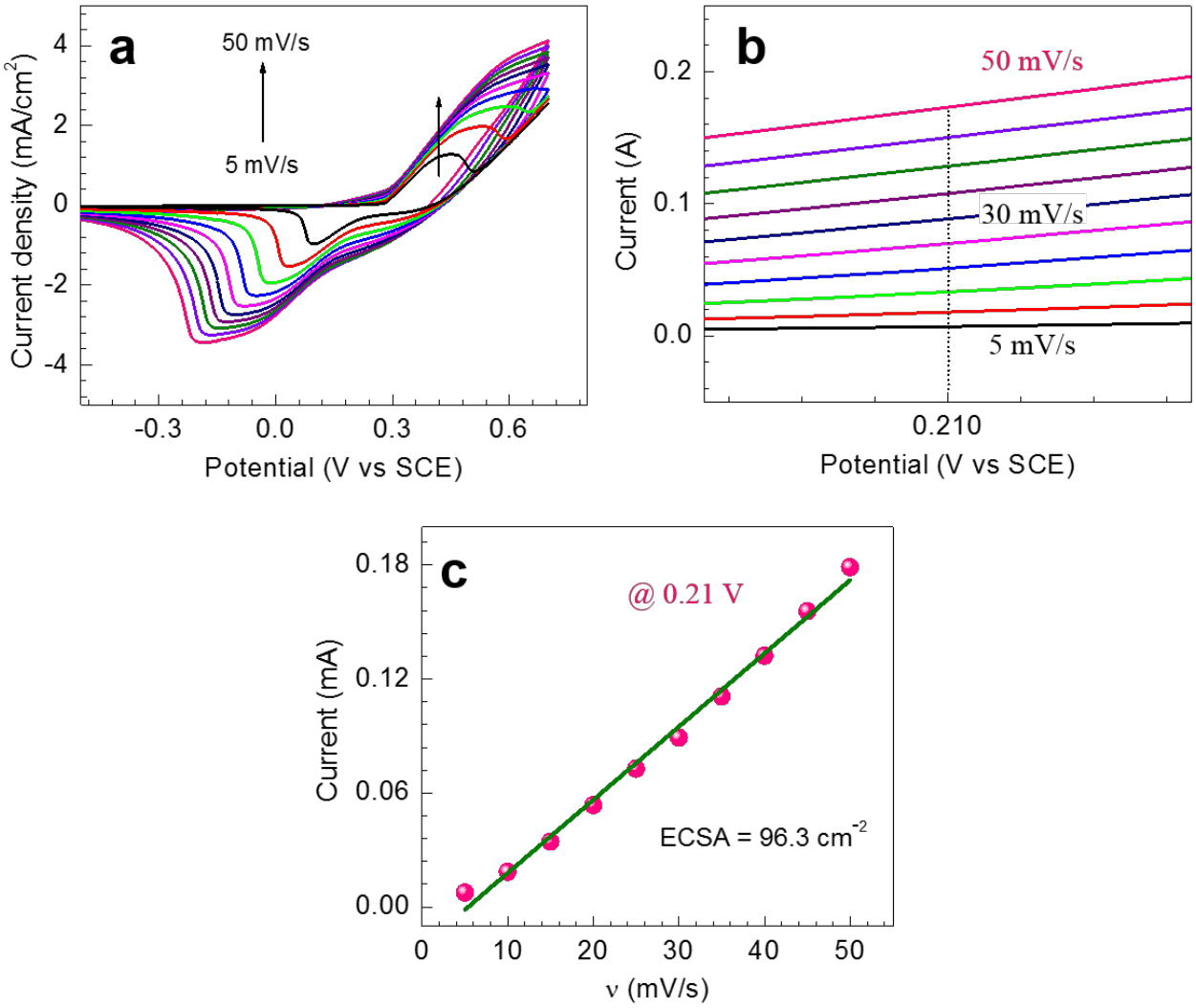

Fig. 6. (a) Cyclic Voltammogram (CV) of the $NiMoO_4$ electrode at various scan rates. (b) Non-faradaic current in the low potential region for various scan rates (ν). (c) Capacitive current (I_{DL}) measured at 0.21 V, as a function of scan rate.

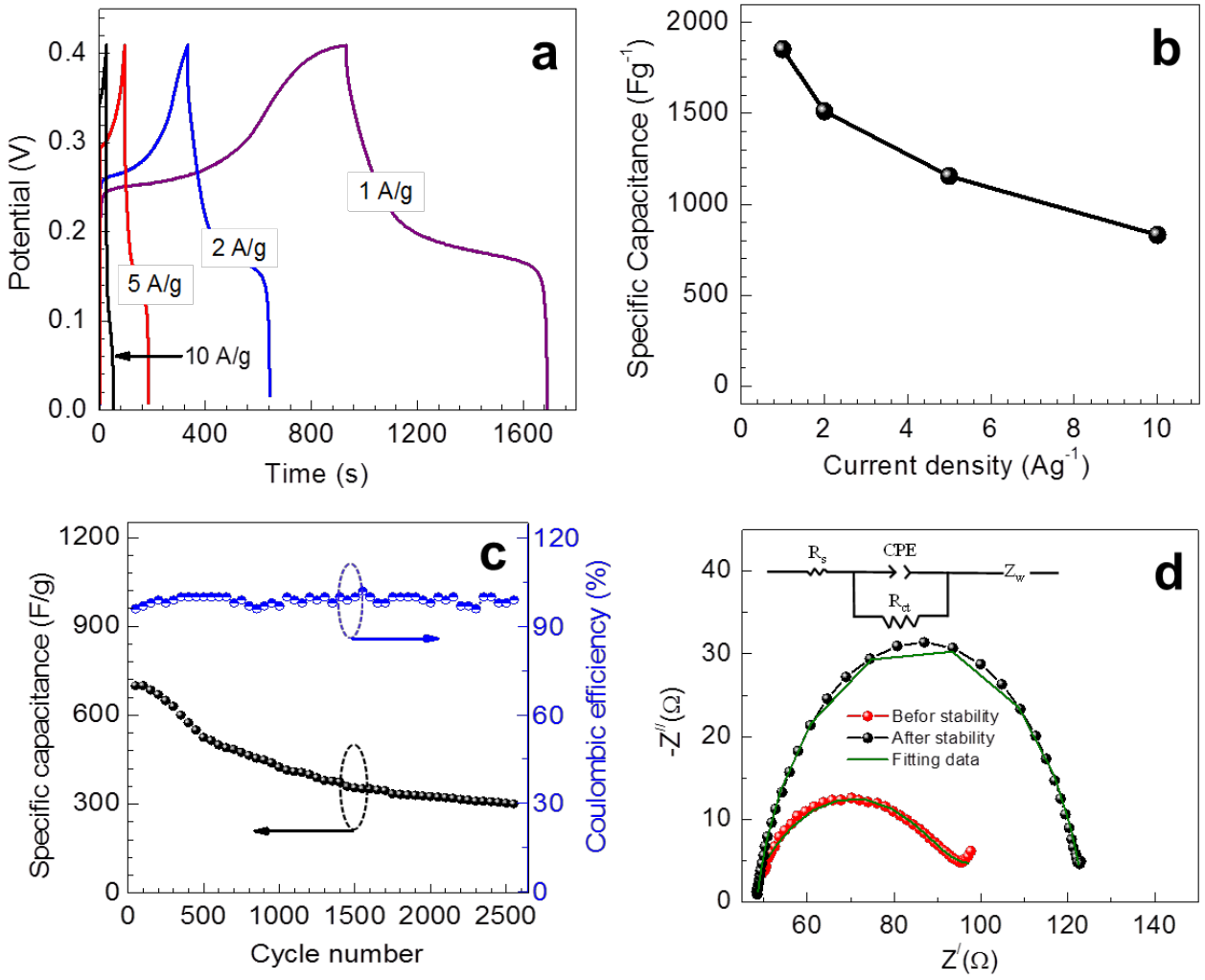

Fig.7. (a) Galvanostatic charge-discharge (GCD) curves of the $NiMoO_4$ electrode at various current densities. (b) Specific capacitance, obtained from the GCD curves at various current densities. (c) Cycling stability test at a high current density of 10 Ag^{-1}. (d) Nyquist plot before and after the cycling test.

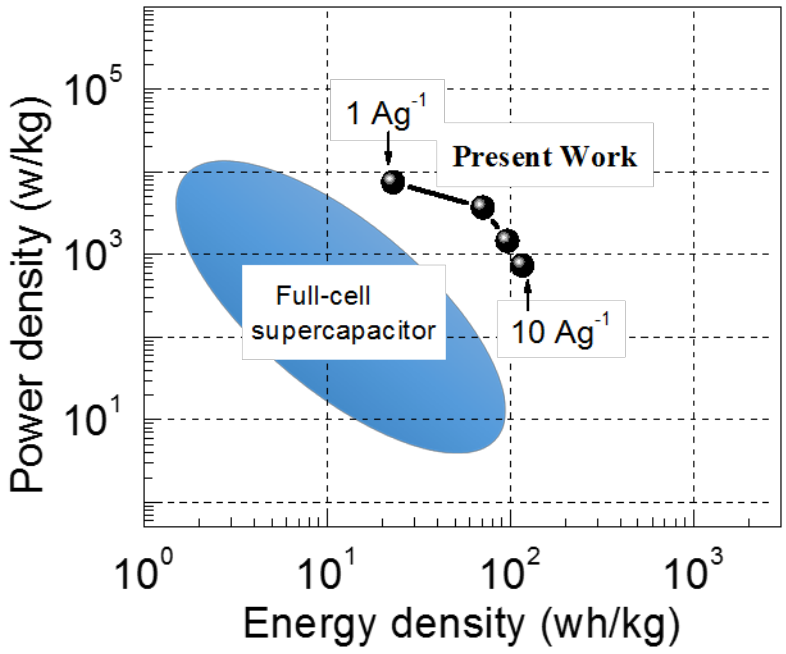

Fig. 8. Calculated energy and power densities (Ragone plot) for the $NiMoO_4$ electrode at various charge/discharge current densities.